Advanced Functional Materials

ADVANCED FUNCTIONAL MATERIALS
www.afm-journal.de

RESEARCH ARTICLE

Incorporation of One-Dimensional Copper Idione (1D CuI) Chains Within Bimetallic Coordination Frameworks for No_2 Sensing

Zi-Wei Li[1] | Zu-Wu Tang[2] | Ke Zhao[3] | Bin Tan[3] | Liang-Xiao Tan[3] | Xiao-Ying Huang[1] | Gang Xu[1] | Wei Zhang[2] | Zhao-Feng Wu[1]

[1]Fujian Institute of Research on the Structure of Matter, Chinese Academy of Sciences, Fuzhou, Fujian, P. R. China | [2]School of Materials and Packing Engineering, Fujian Polytechnic Normal University, Fuzhou, China | [3]School of Chemistry and Chemical Engineering, Beijing Institute of Technology, Beijing, P. R. China

Correspondence: Wei Zhang (zhangwei@fpnu.edu.cn) | Zhao-Feng Wu (zfwu@fjirsm.ac.cn)

Received: 15 September 2025 | **Revised:** 12 January 2026 | **Accepted:** 12 January 2026

Keywords: 1D chain | bimetallic coordination assembly | chemresistive sensing | coordination polymer | CuI

ABSTRACT

This study introduces a bimetallic alkali-metal coordination assembly approach to modulate the structural configurations of copper iodide (CuI) units within various Li-A-CuI-INA ($A^+ = Na^+$, K^+, Rb^+, and HINA denotes isonicotinic acid) coordination frameworks. By co-coordinating Li^+ ions with other alkali metal ions (A^+) in competition for binding with INA^-, the 0D discrete CuI clusters found in the monometallic compound of Li-CuI-INA are transformed into extended 1D chain-like CuI modules, which are then stabilized within the resultant bimetallic Li-A-CuI-INA frameworks. Supported by DFT calculations, the Li-Rb-CuI-INA compound, featuring exclusively 1D stair-like $\{Cu_4I_4\}_n$ chains, was synthesized via this bimetallic coordination assembly strategy. This compound exhibits superior chemiresistive sensing performance for NO_2 operating at room temperature (RT), rivaling the most effective sensing materials reported to date. This study highlights a promising strategy for the rational design of high-performing chemiresistive sensing materials through the integration of DFT computational insights with crystal engineering methodologies.

1 | Introduction

The discovery of crystalline materials featuring 1D chain structures has garnered significant interest due to their unique applications in high-precision electron transport, superconductivity, topological insulation, and diverse optoelectronic fields [1–5]. Examples include 1D nano-ribbons, nanotubes, and nanowires fabricated from chalcogenides and bismuth halides, showing distinctive anisotropic characteristics in phenomena such as band crossing, photoluminescence, and tunneling current, among other properties [6–10]. Nonetheless, the synthesis of these 1D materials, whether achieved through top-down exfoliation techniques or bottom-up vapor deposition methods, often faces challenges in precisely controlling their size distribution and morphology [11–16]. The coordination assembly method has been shown to be an effective strategy for integrating inorganic and organic components into a single, unified crystal lattice via coordination interactions [17–21]. This approach generates hybrid structures that integrate 1D inorganic components with organic substances, leading to consistent electron confinement along the 1D chains and improved electron transport properties [22–26]. Unlike conventional methods that rely solely on organic

---

Zi-Wei Li and Zu-Wu Tang contributed equally to this work.

ligands to modify inorganic constituents, metal-organic frameworks (MOFs) or coordination polymers (CPs) offer a diverse array of coordination possibilities between metal ions and organic linkers [27–30]. The versatility in coordination results in numerous distinct coordination sites and confined environments, thereby conferring structural adaptability to inorganic components. However, the utilization of metal–organic coordination assemblies for the precise manipulation of inorganic component structures remains insufficiently explored [31–34].

Copper iodide (CuI), a prominent representative of metal halides, is extensively employed in a variety of optoelectronic applications, including but not limited to piezoelectric devices, photodetectors, and transparent transistors [35–38]. CuI exhibits distinct properties that are contingent upon its structural configuration across three principal phases. These phases offer a variety of structural features that facilitate the development of crystalline hybrid materials [39, 40]. Consequently, CuI represents an outstanding functional constituent that can be incorporated into CPs to investigate novel properties arising from its structural characteristics [41–43]. Although numerous studies have examined CPs containing CuI motifs, these investigations predominantly focus on their structural characteristics and provide limited insight into their physical properties [44–46]. We first developed a coordination assembly method to precisely manipulate the structural configurations of CuI modules within diverse K-INA-R frameworks by regulating the organic ligands. This strategy enabled the optimization of sensing performances to NO_2 by controlling the dimensionality of CuI components in these K-INA-R CPs [47]. However, modifying the functional groups of organic ligands to tailor the structural properties of CuI frequently remains a critical challenge in organic synthesis. Owing to the differences in atomic radii and coordination behaviors among alkali metals (A^+), the introduction of various A^+ ions to compete for coordination with the ligands represents a promising approach to tailor the structural features, dimensionality, and sensing properties of CuI within alkali-metal-containing CPs.

Bearing this in mind, we have successfully synthesized a notable series of CuI-incorporated bimetallic Li-A-CuI-INA coordination networks, achieved by the incorporation of heterometallic alkali cations ($A^+ = Na^+, K^{+,}$ and Rb^+). These structures offer diverse coordination environments for alkali metals and create confined spaces for accommodating CuI modules with varying dimensionalities, spanning from 0D clusters to extended 1D chain structures encapsulated within the assembled frameworks (Scheme 1). The compound of Li-Na-CuI-INA containing both 1D $\{Cu_6I_5\}_n^+$ and $\{Cu_5I_4\}_n^+$ chains shows superior chemiresistive sensing performance to NO_2 operating at room temperature (RT), outperforming the sensing capabilities of Li-CuI-INA and, notably, the pristine CuI working at an elevated operating temperature of 240°C [48, 49]. However, the issues of slow recovery and poor recyclability, which are common issues for CP sensing materials, have impeded their potential applications. DFT calculations were conducted on the Li-Na-CuI-INA system, indicating the 1D $\{Cu_6I_5\}_n^+$ chains exhibit a stronger interaction with NO_2, as evidenced by a higher adsorption energy, compared to that of the $\{Cu_5I_4\}_n^+$ chains formed through double Cu–I bonds. Subsequently, Rb^+ ions with larger radius and more abundant coordination numbers was introduced to further modulate the coordination environments between Li^+ and HINA, yielding the Li-Rb-CuI-INA containing exclusively 1D stair-case $\{Cu_4I_4\}_n$ chains with a compratively moderate adsorption energy to NO_2. Li-Rb-CuI-INA performed the best chemiresistive sensing performance to NO_2 with enhanced sensing recovery and recyclability, which are also comparable to the best-performing RT NO_2 sensing materials reported thus far.

2 | Results and Discussion

2.1 | Crystal Structure

The incorporation of Li^+ alongside another alkali metal ion (Na^+, K^+, or Rb^+), which engages in both cooperative and competitive coordination with the carboxylate group of the INA- ligand, enables precise structural modulation of bulk CuI. The INA- ligand selectively donates its pyridine (py) coordination site to Cu(I), facilitating the transformation of bulk CuI into 0D clusters as well as 1D linear and staircase-like chain architectures (Scheme 1). These binding modes facilitate the targeted localization and confinement of CuI modules within the periodically ordered bimetallic CPs. In the Li-CuI-INA compound, Li^+ exhibits tetrahedral coordination with oxygen atoms derived from carboxylate groups, a coordination environment that has been frequently reported in prior studies (Figure S1a). Each Li^+ ion is bridged by four carboxylic groups to connect the same six adjacent Li^+ ions, forming a continuous Li-COO chain (Figure S1c). The pyridine moieties are anchored on either side of the metal-carboxylate chain, establishing a confined environment that facilitates the formation of two distinct types of clusters, namely $\{Cu_5I_5\}_n$ and $\{Cu_4I_3\}^+{}_n$. These clusters are encapsulated within the resulting 3D Li-CuI-INA framework (Figure S1b–e).

In the case of Li-Na-CuI-INA (Figure 1a), the incorporation of Na^+, which has a larger radius and higher coordination numbers compared to Li^+, significantly alters the coordination environment surrounding Li^+ ions. Na^+ can be five- or six-coordinated by four different COO^- groups, in both mono- and bidentate fashion (Figure S2a). This contrasts with Li-CuI-INA, where Li^+ is four-coordinated solely with four carboxylic groups (Figure S1a). The co-occurrence of Li^+ and Na^+ ions in the same spatial positions within the crystal lattice, displaying coordination numbers of five-, six- or seven, leads to the formation of a mixed bimetallic $\{Li\text{-}Na\text{-}COO\}_n$ layer (Figure S2b). The modifications in the coordination environment of Li^+ alter the spatial conformation and influence the organization of free pyridines. As a result, two types of 1D CuI chains are generated, one of which is assembled with $\{Cu_6I_5\}_n^+$ segments by sharing one I atom as a vertex, while the other is built from $\{Cu_5I_4\}_n^+$ segments connected by a double Cu—I bond (Scheme 1, Figure 1b and Figure S2c). These mixed 1D chains are assembled into the 3D framework of Li-Na-CuI-INA formulated as $\{Li_{6.27}Na_{8.73}Cu_{14}I_{11}(INA)_{18}\cdot DMF\}$, making the first example of assembling two types of 1D CuI chains into one host CP framework (Figure S2). This highlights the distinctive advantages of bimetallic coordination assembly in modulating the structures of CuI.

Notably, with the augmentation of the structural dimensionality of CuI from 0D clusters in Li-CuI-INA to the 1D chains, the Li-Na-CuI-INA demonstrates a pronounced sensitivity in detecting NO_2 within the range of 1 to 100 ppm at RT (Figure 1c and

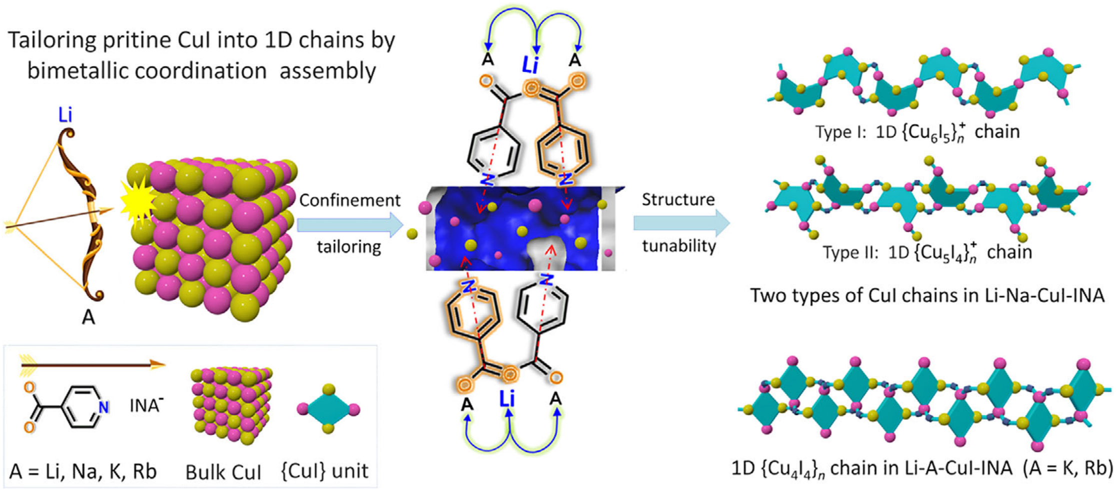

SCHEME 1 | The schematic figure for the bimetallic coordination way to tailor CuI into 1D chains.

Figure S3), showing a milder working condition than that of the pristine CuI at 240°C [48, 49]. However, it displays a significantly larger response CV of 28.80% (Figure S4), indicating its poor repeatability and reliability. Additionally, the recovery time for Li-Na-CuI-INA toward 10 ppm NO_2 is also more than 10 min, which would also hinder its further applications (Inset of Figure 1c). DFT calculations were conducted on Li-Na-CuI-INA, revealing that the Cu(I) sites in 1D $\{Cu_6I_5\}_n{}^+$ chains can excessively interact with NO_2 with a high adsorption energy of −2.03 eV, while the 1D $\{Cu_5I_4\}_n{}^+$ chains fabricated from the double Cu-I edges exhibit a moderate energy value of −1.79 eV (Figure 1d and Figure S5). The high adsorption energy means the release of NO_2 adsorbed onto the 1D $\{Cu_6I_5\}_n{}^+$ chains in Li-Na-CuI-INA is more challenging, causing the weak sensing repeatability and slow recovery. Both the experimental and DFT results indicate that the gas sensing performances of these CPs are not only dependent on the structure dimensionality of CuI modules but also involve the bridging modes between each CuI segment. Therefore, removing the 1D $\{Cu_6I_5\}_n{}^+$ chains with high gas adsorption energy while retaining exclusively the chains that contain double Cu—I bonds in the host framework would help optimize its sensing recovery and recycling capacity.

Subsequently, K^+ or Rb^+ ions with larger ionic radii and a greater diversity of coordination modes were introduced to further alter the structural properties of the CuI modules. By using Rb^+ or K^+ ions to competitively coordinate with HINA, only the 1D $\{Cu_4I_4\}_n$ chains formed by sharing the double Cu—I bond are solely formed in Li-K-CuI-INA and Li-Rb-CuI-INA, respectively (Figure 1e). In Li-K-CuI-INA, Li^+ adopts a tetra-coordinated way while K^+ ions adopt six- or seven-coordinated ways, respectively (Figure S6a). The Li^+ and K^+ ions bridge with COO^- to form a 2D $\{Li_2K(INA)_4\}_n$ layer (Figure S6b). The pyridines from INA^-, projecting on both sides of the $[Li_2K\text{-}(INA)_4]_n$ plane along *a* axis, act as a structural guide to direct the assembly of CuI into staggered, parallel arrays (Figure S6c). Due to the spatial arrangements dictated by the pyridines, an extended 1D stair-case-like chain assembled with $\{Cu_4I_4\}_n$ segments through forming a double Cu—I bond is generated and confined into the 3D hybrid of $\{Cu_5I_4CuK_4Li(INA)_6\}_n$ (Figure S6c,d). By increasing the heterometal radius and coordination numbers from K^+ to Rb^+, a compound of Li-Rb-CuI-INA, namely $\{Cu_5I_4Rb_4Li(INA)_6\}_n$ featuring the same structure as Li-K-CuI-INA, is obtained. Rb^+ mirrors the coordination modes of K^+ ions in Li-K-CuI-INA, forming the identical 1D $\{Cu_4I_4\}_n$ chain as that confined in Li-K-CuI-INA (Figure 1e and Figure S7).

The versatility of the bimetallic coordination method is further showcased by combining Na^+ and Rb^+ to coordinate with INA^- to intricately tune the structures of the 1D CuI modules. In Na-Rb-CuI-INA of $\{(Cu_4I_4)CuNa_{2.2}Rb_{2.8}(INA)_6\}_n$, Na^+ and Rb^+ ions, similar to that of Li^+ and Rb^+ pairing in Li-Rb-CuI-INA, adopt abundant coordinated numbers to coordinate with COO^- groups. Na^+ ions are tetra- or hexa-coordinated while Rb^+ ions are seven- or eight-coordinated along with the increasing of its radius (Figure S8a). Each Na^+ ion is linked to the neighboring Rb^+ ions with COO^- groups to form a $\{Na\text{-}Rb\text{-}COO\}_n$ layer (Figure S8b). The pyridines anchored on both sides of the layers coordinate with CuI in a nearly identical manner (Figure S8c). As a result, the same 1D staircase-like CuI chain is observed as that in Li-K-CuI-INA and Li-Rb-CuI-INA (Figure S8d). This demonstrates that the structural variations of CuI are predominantly influenced by the bimetallic ions with differences in radius and coordination numbers. Taking Li^+ as an instance, it typically adopts tetra-coordination modes to coordinate with the carboxylic group in its pristine CP structures [50]. By incorporating Na^+, K^+, or Rb^+ ions with larger radius and more abundant coordination numbers [51, 52], the coordination configurations of Li^+ are adjusted, favoring the formation of 1D CuI chains with new structure features. These findings highlight that the bimetallic coordination is an effective method to tailor the structural features of CuI, suggesting its broader applicability in the design of novel hybrids bearing the functional inorganic modules.

2.2 | Physical Characterizations

The purity and the thermal stabilities of the samples are measured through PXRD, EA, and TG characterizations (Figures S9–S18). The electronic structures of these hybrids are also studied (Figures S19–S22). Taking the monometallic CP of Li-CuI-INA as an example, the valence band maximum (VBM) is primarily composed of the Cu 3d and I 5p atomic orbitals

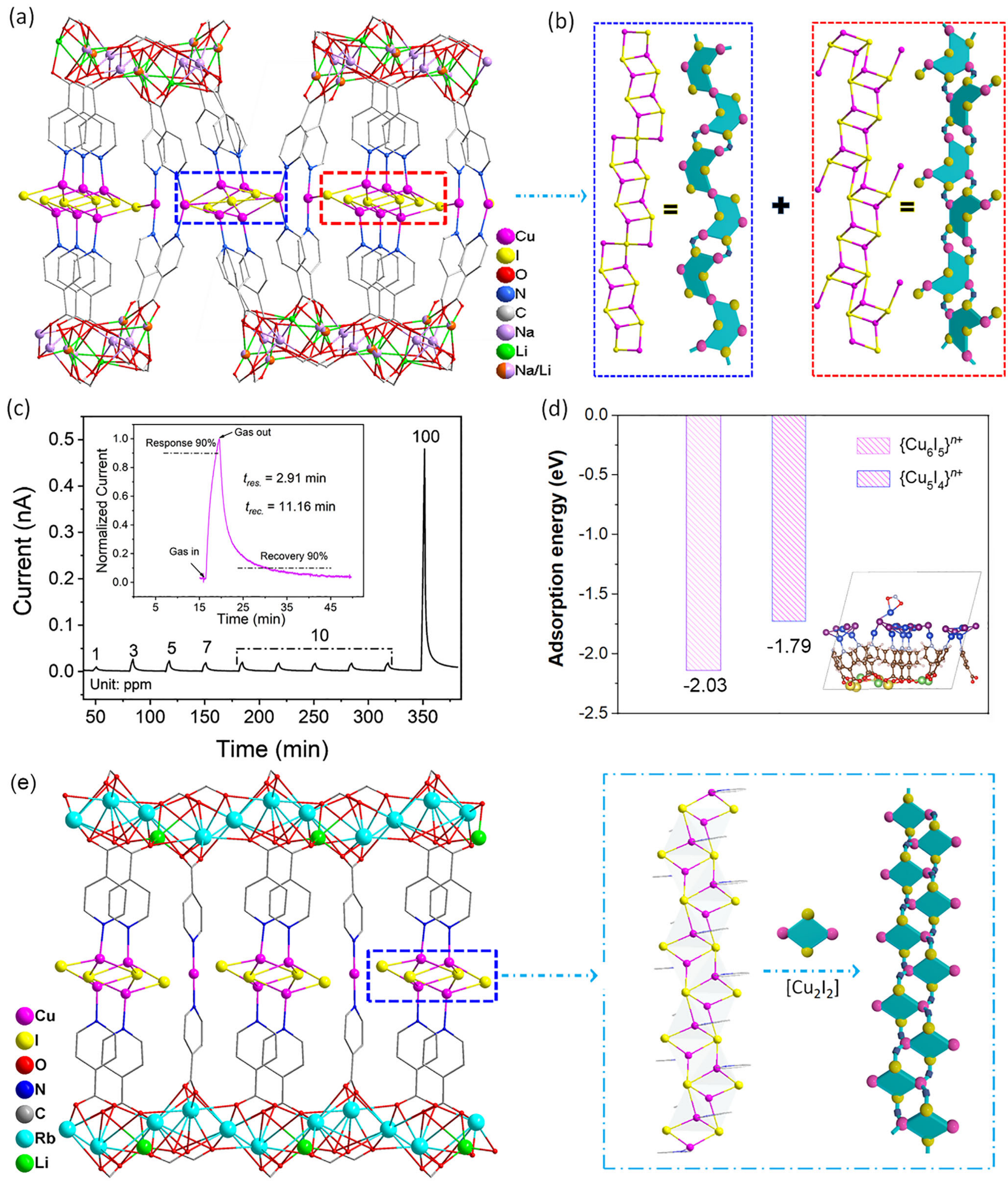

FIGURE 1 | (a) The 3D structure of Li-Na-CuI-INA. (b) The mixed 1D $\{Cu_6I_5\}_n{}^+$ and $\{Cu_5I_4\}_n{}^+$ chains in Li-Na-CuI-INA, highlighted with dotted red and blue lines, respectively. (c) Response and recovery curve for Li-Na-CuI-INA toward NO_2 with different concentrations at RT. Inset: The sensing response and recovery time toward 10 ppm NO_2. (d) Adsorption energy of NO_2 with CuI motifs in Li-Na-CuI-INA from DFT calculations. Inset is the illustration of DFT calculation of NO_2 adsorbing to Cu atom with a favorable bidentate O, O′-nitrito binding way. (e) The 3D framework of Li-Rb-CuI-INA with the 1D staircase-like $\{Cu_4I_4\}_n$ chain highlighted in a dotted blue line. The same 1D $\{Cu_4I_4\}_n$ chain is also seen in the bimetallic compounds of Li-K-CuI-INA and Na-Rb-CuI-INA, respectively.

from the CuI clusters, while the conduction band minimum (CBM) predominantly arises from the 2p orbitals of C, N, and O atoms in the INA$^-$ ligand (Figure S19). Regarding bimetallic compounds, such as Li-Na-CuI-INA, both the VBM and CBM are similarly composed of elements from the inorganic CuI motifs and organic ligand, respectively (Figure S20). This result indicates that the A$^+$ ions primarily influence the structural arrangements of the CuI modules. Interestingly, transforming bulk CuI into building segments for the assembly of 1D chains with distinct structural features also results in the tuning of their band gaps. Unlike the pristine CuI with a wide band gap (>3.0 eV), the adsorption of these resultant hybrids falls within the visible light region, featuring relatively narrow band gaps (Figures S23–S27). The photoconductivity of these hybrids was measured and analyzed comparatively (Figures S28–S32), ranging from 10^{-11} to 10^{-8} A that correlate with the structure dimensionality transition of CuI modules from 0D clusters to 1D chains. The pristine Li-CuI-INA containing 0D clusters exhibits relatively low conductivity on the order of 10^{-11} A (Figure S28). In contrast, the bimetallic compounds of Li-A-Cu-CuI (A = Na, K, Rb) and Na-Rb-CuI-INA with 1D CuI chains display significantly enhanced conductivities, ranging from 10^{-10} to 10^{-8} A (Figures S29–S32). Additionally, these compounds exhibit temperature-dependent conductivity, with higher values corresponding to the elevated temperatures (Figures S33–S37 and Table S3). The strong linearity observed between Lnσ and 1000/T for these compounds confirms their semi-conductive natures. Temperature-dependent conducting behaviors for these Li-A-CuI-INA compounds demonstrate a typical Arrhenius-type response, indicating that charge transport is driven by thermally activated conduction processes [53, 54].

The compounds of Li-CuI-INA, Li-Na-CuI-INA, and Li-Rb-CuI-INA possess rod-like crystal morphology in mm sizes (Figures S38–S41), allowing the investigation of their anisotropic properties through the direct current two-terminal method on selected single-crystals (Figure 2a and Figure S42–S44). As depicted in Figure 2b and Figure S42, the single crystal sample of Li-CuI-INA exhibits similar conductivity magnitudes when measured along both the long and short sides of the rod crystal, demonstrating no anisotropic character for the Li-CuI-INA. This absence of anisotropy aligns with its 0D CuI cluster structural features. In contrast, Li-Na-CuI-INA and Li-Rb-CuI-INA bearing the 1D CuI chains demonstrate a classic anisotropic conducting behavior (Figure 2c,d). Taking Li-Rb-CuI-INA as an example, the conductivity along the long side of the crystal (inset of Figure 2d, aligned with the direction along the 1D $\{Cu_4I_4\}_n$ chains in the crystal structure) is measured as 2.88×10^{-9} S/cm. This is at least an order of magnitude higher than the 1.67×10^{-10} S/cm recorded along the short side (perpendicular to the 1D $\{Cu_4I_4\}_n$ chain). As the testing temperature increased from 303 to 413 K, the conductivity for Li-Rb-CuI-INA, measured along a axis, reached a peak value of 1.34×10^{-6} S/cm (Figure S44). The conductivity of 1.34×10^{-6} S/cm is comparable to that of CuI-L hybrid of $Cu_4I_6(bttmp)_2$ (2.8×10^{-6} S/cm) [55] and CuI-K-INA (1.21×10^{-6} S/cm) with 2D CuI layers in our previous work [47], and orders higher than that of the perovskite crystals by using the same measuring method [56–58]. Similar anisotropic conducting behaviors, following the same trend was also observed in Li-Na-CuI-INA with the 1D CuI chains (Figure 2c).

2.3 | NO_2 sensing performance

DFT calculations reveal that the adsorption energy of NO_2 to Cu atoms from $\{Cu_4I_4\}_n$ chains in Li-K-CuI-INA and Li-Rb-CuI-INA is reduced to about -1.78 eV and -1.65 eV, respectively (Figure S45). A Bader charge analysis was conducted on the NO_2-adsorbed structures, revealing that the reduced charge transfer observed in Li-K-CuI-INA and Li-Rb-CuI-INA systems further suggests moderate interactions between the CuI modules and the NO_2 molecules (Figures S46–S47). The lower adsorption energy and charge transfer indicate that their sensing recovery and recycling capacity might be optimized. As depicted in Figure 3a, Li-K-CuI-INA, Li-Rb-CuI-INA, and Na-Rb-CuI-INA with the same staircase-like $\{Cu_4I_4\}_n$ chains, created by bridging CuI segments with the double Cu—I bonds, show similar NO_2 sensing performances compared with each other while exhibiting much better sensing capacities than that of Li-Na-CuI-INA (Figures S48–S50). The response CV values of 2.73%, 4.20%, and 5.60% for these compounds are much lower than that of Li-Na-CuI-INA with the mixed 1D CuI chains (28.80%), indicating their better sensing repeatability and reliability (Figure 3a). As depicted in Figure 3b, the recovery time for the Li-K-CuI-INA, Li-Rb-CuI-INA, and Na-Rb-CuI-INA toward 10 ppm NO_2 is much faster than that of Li-Na-CuI-INA, indicating their sensing recovery performance is also optimized through structure modifications of CuI modules. Li-Rb-CuI-INA, which bears the identical 1D stair-like CuI chain observed in both Li-K-CuI-INA and Na-Rb-CuI-INA, serves as a representative model to comprehensively demonstrate their sensing capabilities to NO_2. The average responses (R_{avg}) of five fabricated sensing devices to 100 ppm NO_2 of Li-Rb-CuI-INA were remarkably high, reaching 2831%, despite the presence of other 100 ppm interfering gas analytes (Figure 3c). Upon exposure to NO_2, the conductance of Li-Rb-CuI-INA significantly increases, and then recovers to the initial value when purged with dry air. Li-Rb-CuI-INA also shows consistent dynamic response-recovery behavior to NO_2 across a broad concentration range of 1–100 ppm, exhibiting a similar concentration-dependent trend in their responses and the best sensing repeatability among the studied compounds (Figure 3d). For 10 ppm NO_2, the response and recovery times are 68 and 103 s, respectively (Figure S49). These values represent a halving of the response (121.8 s) and recovery (212.3 s) times recorded for CuI-K-INA under the light illumination in our previous work [47], highlighting the superior sensing performances of Li-Rb-CuI-INA. Additionally, the limit of detection (LOD) for Li-Rb-CuI-INA is calculated to be 9.39 ppb and a coefficient of determination of 0.996, comparable to CuI-K-INA (1.12 ppb) with 2D CuI layers and other high-performing sensing materials, Figure 3e [59–71]. Li-Rb-CuI-INA represents one of the best NO_2 sensors reported to date (Figure 3f and Figure S51) [59–71]. For a thorough comparison, other NO_2 sensing compounds, including oxides, sulfides, carbon complexes, and other CP-based sensing materials, are also listed in Table S4. Li-Rb-CuI-INA can maintain its 95% sensing response toward 10 ppm NO_2 after more than one month, indicating its long-term sensing stability (Figure S52). The sensing response to NO_2 under different relative humidity (RH) levels exhibited negligible variation, indicating its robustness and reliability in practical environmental conditions (Figures S53 and S54). As illustrated in Figure S55, crystals with relatively larger sizes, which are more susceptible to orientation effects, exhibited a slightly reduced

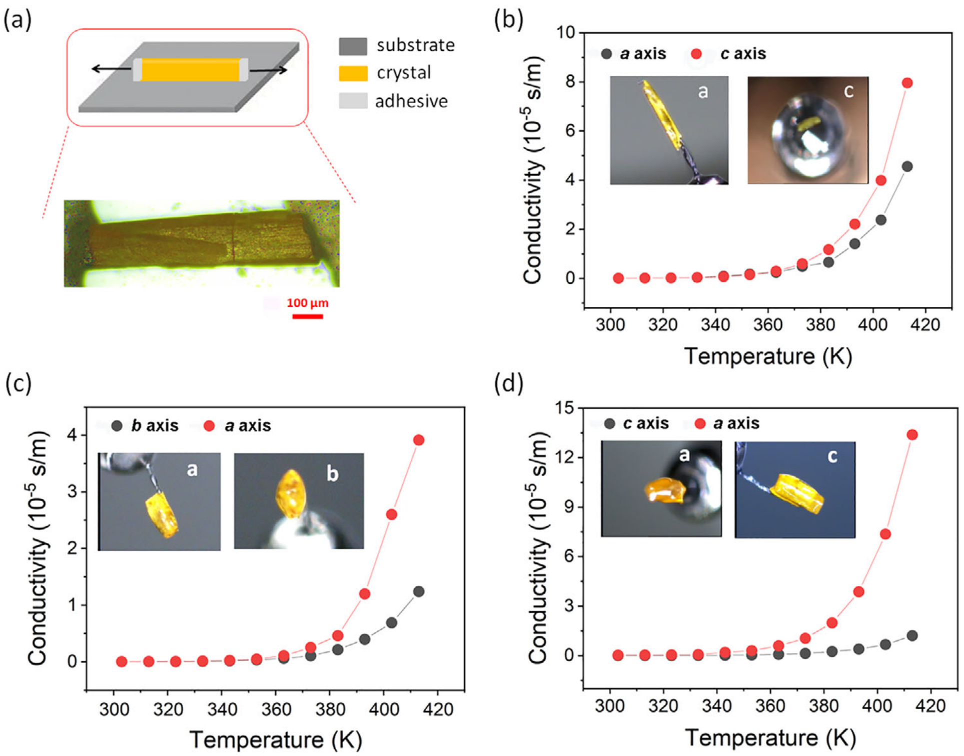

FIGURE 2 | (a) The anisotropic conductivity measurements by the direct current two-terminal method on selected single-crystals. Inset is the photograph of the single crystal of Li-CuI-INA used for anisotropic conductivity study along the long side of the single crystal sample. Scale bar: 100 μm. (b) The temperature-dependent conductivity for Li-CuI-INA along the *b* and *c* axis of the single crystal. (c) The temperature-dependent conductivity for Li-Na-INA along *b* and *c* axis of the single crystal. (d) The temperature-dependent conductivity for Li-Rb-INA along *b* and *c* axis of the single crystal. The insets are their crystal photographs viewed along the same directions as those in measuring the anisotropic conductivities.

sensing response (Figure S55b,d). Developing sensing membranes with a uniform crystal orientation to further enhance the NO_2 sensing performance would be carried out in our lab in the future.

2.4 | Mechanism study

The CPs bearing the 1D $\{Cu_4I_4\}_n$ chains demonstrate the best sensing performances, making Li-Rb-CuI-INA a prime candidate for detailed investigation of the sensing mechanism. The projected density of states (PDOS) for the Li-Rb-CuI-INA compound before and after the adsorption of NO_2 was calculated. Subsequent to NO_2 adsorption, a significant shift of the Fermi level toward the valence band states was observed, indicative of p-type doping behavior in the semiconductor material. This finding implies that the NO_2 molecule induces the formation of gap states during the sensing process [72, 73]. As depicted in Figure S57, the Fermi level of Cs-CuI-K-INA deviates from the middle of the band gap and is close to the valence band (VB), which further suggests Cs-CuI-K-INA is a p-type semiconducting material [74, 75]. The conductivity of Li-Rb-CuI-INA increased rapidly upon exposure to different concentrations of NO_2, which is also a typical p-type semiconductor behavior. In our study, Cs-CuI-K-INA is a crystal compound, and the high crystal quality is beneficial to reducing carrier scattering, thereby increasing carrier mobility [76–79]. When the sensor is exposed to NO_2, the high-speed carrier transport channel is greatly broadened due to the fact that a large number of electrons are captured by NO_2, leading to a significant increase in the entire carrier mobility and conductivity. The PXRD measurements of the sample after NO_2 sensing confirmed that the structures remain unchanged, suggesting the NO_2 sensing response was not caused by structure collapse (Figures S58–S61). Then, time-resolved diffuse reflectance infrared Fourier transform spectroscopy (DRIFTS) measurement has been conducted. Notably, upon exposure to NO_2, new spectral bands appeared, compared with those of the pristine sample depicted in Figure 4a. These new peaks continuously intensified with prolonged exposure time, indicating the presence of species resulting from NO_2 interaction with the sample surface [80–82]. The adsorbed NO_2 can be identified by its ν_{as} band around 1720 cm^{-1}, displaying a blue shift from its gas phase value of 1620 cm^{-1} [83–85]. This shift is attributed to partial electron donation to the sample surface, resulting in the stiffening of the N═O bond. Besides, three distinct new peaks, labeled as I), II), and III), respectively, are the characteristic bands of nitrate species (NO_3^-). They correspond to the N═O stretching and the asymmetric/symmetric stretching vibrations of the $-NO_2$ group within NO_3^- ions [86, 87]. In addition, the characteristic broad band around 1800–1900 cm^{-1} for NO is also observed, which corresponds to its stretching vibration of nitrosyl species formed on the cationic sites (Figure 4a) [86]. In order to confirm this sensing mechanism across hybrids with identical 1D CuI chains, the DRIFTS of Na-Rb-CuI-INA is also measured, revealing new peaks at the same positions, which are in accordance with their similar sensing performances (Figure S62). XPS measurements are also performed on the sample both before and after NO_2 exposure. As shown in Figure 4b, the N 1s spectrum shows a minor shoulder peak around 406 eV after exposure, typically indicating

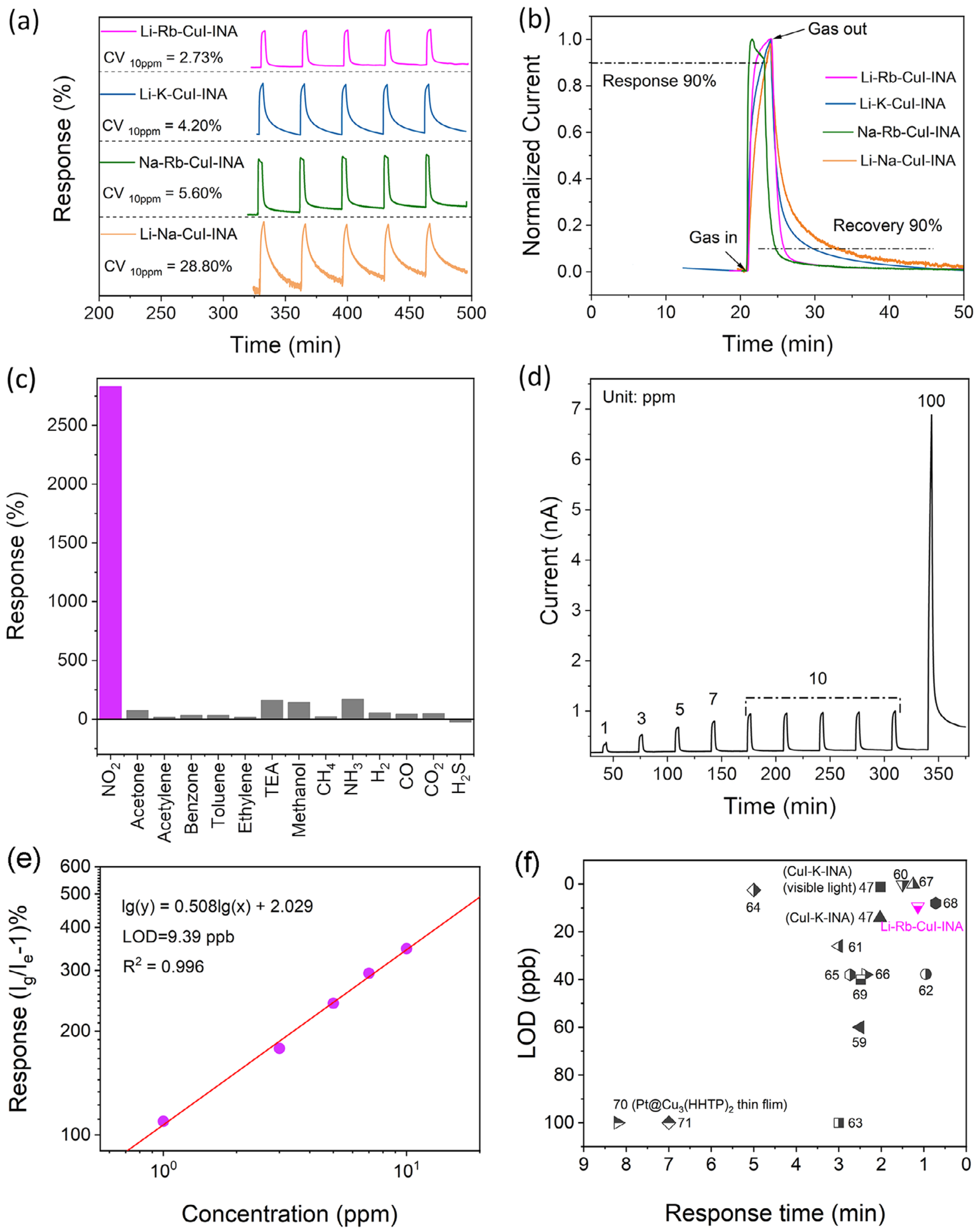

FIGURE 3 | (a) Coefficient of variation for cycle testing of Li-M-CuI-INA (M = Na, K, and Rb) and Na-Rb-CuI-INA toward 10 ppm NO_2. (b) Sensing recovery time of Li-M-CuI-INA (M = Na, K, and Rb) and Na-Rb-CuI-INA. (c) Responses of Li-Rb-CuI-INA as sensors to 100 ppm NO_2, together with other interference gases. (d) Response and recovery curve of Li-Rb-CuI-INA toward NO_2 with different concentrations at RT under dark conditions. (e) Log–log linear fitting of the response-concentration plot. (f) The selected reported NO_2 sensing complexes containing response time and LOD values as references.

NO_3^- ions [88], further supporting the DRIFTS findings of NO_3^- formation on the sample surface. A potential reaction pathway for the conversion of NO_2 to nitrate was also proposed; the energetic analysis of species with different adsorbed configurations indicated that this process is energetically favorable (Figure S63) [80, 89, 90]. The energy barrier associated with the adsorption and desorption of NO_2 on the 1D $\{Cu_4I_4\}_n$ chain within Li-Rb-CuI-INA was calculated to 0.76 eV, which is lower than the corresponding barrier of 1.05 eV observed for the 1D $\{Cu_6I_5\}_n^+$ chain in Li-Na-CuI-INA based on the same procedure. This value also explains the faster sensing and recovery rates for Li-Rb-CuI-INA through tuning the structure features of the CuI modules. Based on the discussions above, the sensing mechanism can be conceptualized as a Lewis acid–base interaction occurring between the CuI

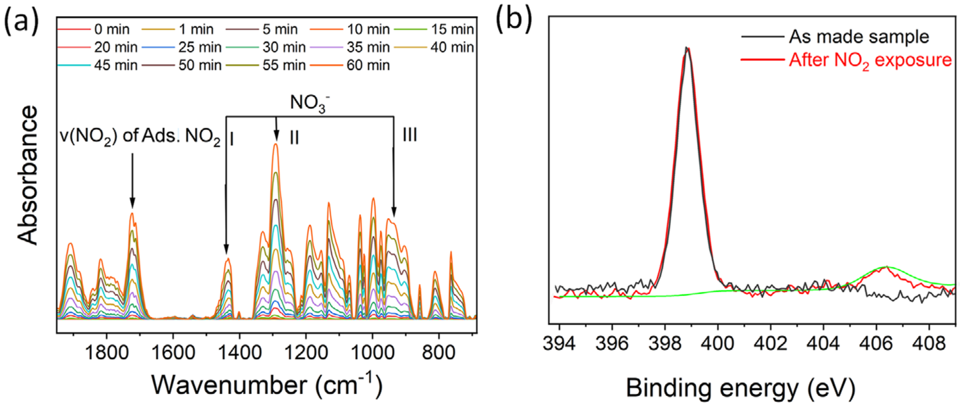

FIGURE 4 | (a) Time-resolved DRIFTS spectra of Li-Rb-CuI-INA during NO_2 sensing. (b) The XPS spectra of N1s in Li-Rb-INA-CuI before and after NO_2 exposure.

module and NO_2: $2NO_2(ads) \rightarrow NO_3^-(ads) + NO(gas)$ [47, 91, 92]. The significant change in resistance is ascribed to the substantial electron transfer from the CuI sites to the NO_2 molecules.

3 | Conclusions

In summary, the use of a bimetallic coordination assembly approach led to the successful preparation of a series of bimetallic CPs bearing 1D CuI chains. By tailoring the pristine CuI into 1D conductive segments and integrating them into these bimetallic CPs, the compounds offer selective and sensitive chemiresistive sensing for NO_2 at RT, without requiring light exposure, and show significant improvements in sensing capabilities (such as sensitivity, selectivity, and LOD) compared to bulk CuI. Notably, Li-K-CuI-INA, Na-Rb-CuI-INA, and particularly Li-Rb-CuI-INA, which all contain the same 1D staircase-like $\{Cu_4I_4\}_n$ chains, emerge as one of the best NO_2 chemiresistive sensing materials reported to date. This work offers valuable insights into the tailored design of new chemiresistive sensing materials with enhanced capacities by modifying their structural characteristics on the basis of the crystal engineering techniques.

4 | Material and Methods

4.1 | Materials

LiI (99%, Adamas Reagent Co., Ltd), NaI (99%, Macklin Inc.), KI (99%, Adamas Reagent Co., Ltd), RbI (99%, Adamas Reagent Co., Ltd), CuI (99%, Adamas Reagent Co., Ltd), 4-Picolinic acid (99%, Adamas Reagent Co., Ltd). All the chemicals were purchased from commercial sources and used without any further purification.

4.2 | Syntheses of Li-CuI-INA

A mixture of CuI (100 mg), LiI (75 mg), INA (100 mg), 3.0 mL DMF, 2.0 mL CH_3CN, and 2.0 mL ethanol was sealed in a 20 mL vessel, heated at 100°C for 3 days, and then cooled to room temperature. The yellow flaky crystals were selected by hand, washed with ethanol, and then dried in the air. Anal. Calc. for $C_{84}H_{71}N_{17}O_{26}Cu_{10}I_8Li_{10}$: C 29.20%; H 2.07% N 6.89%; found: C, 30.83%; H, 2.27%; N, 6.33%.

4.3 | Syntheses of Li-Na-CuI-INA

Li-Na-INA-CuI was synthesized using the same protocol as Li-CuI-INA, except that an additional NaI (75 mg) was used in the reaction. The yield of the light-yellow needle crystals. Anal. Calc. for $C_{111}H_{79}Li_{6.27}N_{19}O_{37}Cu_{14}I_{11}Na_{8.73}$: C, 27.77%; H, 1.66%; N, 5.54%; found: C, 27.76%; H, 1.92%; N, 5.52%.

4.4 | Syntheses of Li-K-CuI-INA

Li-K-INA-CuI was synthesized using the same method as Li-Na-INA-CuI, except that 75 mg of KI instead of NaI was used in the reaction, and the reaction temperature was 100°C. The yield of the orange-yellow rod-like crystals. Anal. Calc. for $C_{36}H_{24}Cu_5I_4K_4LiN_6O_{12}$: C, 25.12%; H, 1.41%; N, 4.48%; found: C, 25.25%; H,1.55%; N,4.96%.

4.5 | Syntheses of Li-Rb-CuI-INA

Li-Rb-INA-CuI was synthesized using the same procedure as Li-Na-INA-CuI, except that 75 mg of RbI instead of NaI was used in the reaction, and the reaction temperature was 100°C. The yield of yellow rod-like crystals. Anal. Calc. for $C_{36}H_{24}N_6O_{12}Cu_5I_4Rb_4Li$: C, 22.68%; H, 1.27%; N, 4.41%; found: C, 22.43%; H, 2.14%; N, 4.57%.

4.6 | Syntheses of Na-Rb-CuI-INA

A mixture of CuI (100 mg), RbI (75 mg), NaI (75 mg), INA (100 mg), 3.0 mL DMF, 2.0 mL CH_3CN, and 2.0 mL ethanol was sealed in a 20 mL vessel, heated at 100°C for 3 days, and then cooled to room temperature. The yield of the orange block crystals was washed with ethanol and then dried in the air. Anal. Calc. for $C_{36}H_{24}Cu_5I_4Na_{2.25}N_6O_{12}Rb_{2.75}$: C 23.44%; H 1.31% N 4.56%; found: C, 23.24%; H, 1.57%; N, 4.56%.

4.7 | Characterization Techniques

Elemental analyses (EA) of C, H, and N were performed using a German Elemental Vario EL III instrument. The UV-vis diffuse reflectance spectra were recorded at room temperature using a Shimadzu UV-2600 spectrophotometer. A $BaSO_4$ plate was used as a standard (100% reflectance). Thermogravimetric analyses (TGA) were carried out with a NETZSCH STA449C at a heating rate of 5°C/min under a nitrogen atmosphere. The Li-Na-INA-CuI of powder X-ray diffraction (PXRD) patterns were obtained from a Miniflex II diffractometer at 30 kV and 15 mA using Cu $K\alpha$ (1.54178 Å) in the angular range of $2\theta = 3–65°$ at room temperature. The Li-CuI-INA, Li-K-CuI-INA, Li-Rb-CuI-INA, and Na-Rb-CuI-INA were conducted on a Rigaku Smartlab X-ray diffractometer with Cu $K\alpha$ radiation (λ = 1.5406 Å) at a scanning speed of 5° min^{-1}. The morphology and microstructure of the fabricated materials were characterized by a field emission scanning electron microscope, JEOL model JSM-6700 FE-SEM, operating at an accelerating voltage of 1.5 or 5.0 kV. The ultraviolet photoelectron spectroscopy (UPS) measurement was performed on the Thermo Scientific K-Alpha electron energy spectrometer with Al $K\alpha$ (1486.6 eV) radiation as the X-ray excitation source.

4.8 | Electrical Conductivity Tests

Electrical conductivity (σ) was obtained by fitting the linear region of the current–voltage curves to Ohm's law. For the bulk sample measurements, the two-contact probe method was used. The single crystal electrodes were made using silver paste and a 50 μm gold line by placing the crystal between two electrodes and connecting it to the semiconductor analysis system (4200SCS, Keithley). The electrical conductivity of the sample was calculated based on Ohm's law. The tests were performed under dark conditions (without any light source), and the temperature change was controlled by the gas sensing station.

4.9 | Gas Sensing Measurements

A 10 mg sample was ground and dispersed in an ethanol solution. Then, the 20 μL as-made sample suspension was directly drip-coated on the interdigital electrode. Last, the obtained electrode was dried at 60°C under vacuum for 6 h before the sensing test. The sensor characterization was shown by a home-made system reported in previous work [93]. The constant gas flow was 600 mL min^{-1}, the bias on the sensor was set to be 5 V, and the current data were recorded using a Keithley 2602B Sourcemeter. Gases with accurate concentration were generated by mixing target gases with dry air in a certain ratio via mass flow controllers (CS-200C, Beijing Sevenstar Qualiflow Electronic Equipment Manufacturing Co., Ltd., China) and then injected into a quartz tube. Responsivity (R): it assesses the influence of NO_2 on responses ($\Delta I/I_0$, I_0 is the current in air, and ΔI represents the change in current in the circuit after exposure to the analyte gas). The coefficient of variation (CV) was estimated by $R_{SD}/R_{avg} \times$ 100%, where R_{SD} and R_{avg}. are the standard deviation (SD) and the average value of responses. The response and recovery times were acquired as the times taken to achieve 90% of the total resistance change.

4.10 | Density Functional Theory (DFT) Calculations

All the calculations were performed in the framework of DFT by using the Vienna ab initio simulation package VASP [94, 95]. The projector augmented wave method was used to describe the interaction between ions and electrons. Electron-electron exchange and correlation interactions have been described by using the Perdew-Burke-Ernzerhof functional (PBE) within the generalized gradient approximation (GGA) [96]. A plane wave basis set with a cutoff energy of 400 eV and a k-point grid generated by the Monkhorst-Pack method were found to give converged results for the surface calculations. The structures were relaxed using either the conjugate gradient algorithm or the quasi-Newton scheme until the forces on all unfixed atoms were less than 0.01 eV/Å. During the geometry optimization, the atoms in the inner two layers are fixed as those in the bulk structure, and the atoms of the two uppermost layers of the surface and the adsorbate are relaxed. It should be noted that the energies of all configurations presented in this work include corrections for dispersion (D3) and ZPE. More details were added in the Supporting Information.

4.11 | DRIFTS Measurement

Time-resolved in situ DRIFTS spectra collection: DRIFTS spectra were collected on a Nicolet 6700 FT-IR spectrometer with MCT/A detector cooled by liquid nitrogen. Data collection was performed on OMNIC software. The KBr was heated to 100°C under a stream of dry synthetic air for 2 h, after which the sample cup was cooled to room temperature and purged with dry synthetic air. After that, a raw absorbance spectrum was collected as background. The sample was processed with the same procedure except 1000 ppm NO_2 was used throughout the test. All spectra were obtained by scanning with a resolution of 4 cm^{-1} from 650 to 2000 cm^{-1}.

4.12 | X-Ray Crystallography

Single-crystal X-ray diffraction data of Na-Rb-CuI-INA, Li-Na-CuI-INA, and Li-K-CuI-INA were collected on a SuperNova Oxford diffractometer with graphite monochromated Mo$K\alpha$ radiation (λ = 0.71073 Å). Single crystal data of Li-Rb-CuI-INA were measured and collected on a Hybrid Pixel Array detector equipped with graphite-monochromated Ga $K\alpha$ radiation (λ = 1.34050 Å) at 298 K. Li-CuI-INA was measured and collected with graphite-monochromated Mo$K\alpha$ (λ = 0.71073 Å) using an XtaLAB Synergy R, HyPix diffractometer at 100 K. The structures were solved by direct methods and refined by full-matrix least-squares on F^2 using the SHELX-2016 program [97]. Non-hydrogen atoms were refined with anisotropic displacement parameters, and the hydrogen atoms bonded to C and N atoms were positioned with idealized geometry. The empirical formulae were confirmed by EA. Detailed crystallographic data and structure-refinement parameters are summarized in Table S1. [CCDC Nos. 2344265–2344268 and 2488044 contain the supplementary crystallographic data for this paper. These data can be obtained free of charge from The Cambridge Crystallographic Data Centre via www.ccdc.cam.ac.uk/data_request/cif.]

Acknowledgements

This work was supported by the National Natural Science Foundation of China (Nos. 22175178 and 22305019).

Conflicts of Interest

The authors declare no conflict of interest.

Data Availability Statement

The data that support the findings of this study are available from the corresponding author upon reasonable request.

References

1. S. Iijima and T. Ichihashi, "Single-shell Carbon Nanotubes of 1-nm Diameter," *Nature* 363 (1993): 603–605, https://doi.org/10.1038/363603a0.

2. K. Liu, J. Deslippe, F. Xiao, et al., "An Atlas of Carbon Nanotube Optical Transitions," *Nature Nanotechnology* 7 (2012): 325–329, https://doi.org/10.1038/nnano.2012.52.

3. R. Nakanishi, R. Kitaura, J. H. Warner, et al., "Thin Single-wall BN-nanotubes Formed Inside Carbon Nanotubes," *Scientific Reports* 3 (2013): 1385, https://doi.org/10.1038/srep01385.

4. Y. Magnin, H. Amara, F. Ducastelle, A. Loiseau, and C. Bichara, "Entropy-Driven Stability of Chiral Single-Walled Carbon Nanotubes," *Science* 362 (2018): 212–215, https://doi.org/10.1126/science.aat6228.

5. R. Xiang, T. Inoue, Y. Zheng, et al., "One-dimensional van der Waals Heterostructures," *Science* 367 (2020): 537–542, https://doi.org/10.1126/science.aaz2570.

6. G.-E. Wang, G. Xu, B.-W. Liu, M.-S. Wang, M.-S. Yao, and G.-C. Guo, "Semiconductive Nanotube Array Constructed from Giant $[Pb^{II}1_8I_{54}$ $(I_2)_9]$ Wheel Clusters," *Angewandte Chemie International Edition* 55 (2016): 514–518, https://doi.org/10.1002/anie.201507083.

7. H. Xu, S. Liu, Z. Ding, et al., "Oscillating Edge States in One-dimensional MoS_2 Nanowires," *Nature Communications* 7 (2016): 12904, https://doi.org/10.1038/ncomms12904.

8. G. Liu, S. Rumyantsev, M. A. Bloodgood, T. T. Salguero, M. Shur, and A. A. Balandin, "Low-Frequency Electronic Noise in Quasi-1D $TaSe_3$ van der Waals Nanowires," *Nano Letters* 17 (2017): 377–383, https://doi.org/10.1021/acs.nanolett.6b04334.

9. R. Noguchi, T. Takahashi, K. Kuroda, et al., "A Weak Topological Insulator State in Quasi-One-Dimensional Bismuth Iodide," *Nature* 566 (2019): 518–522, https://doi.org/10.1038/s41586-019-0927-7.

10. M. K. Ryo Noguchi, Z. Jiang, K. Kuroda, et al., "Evidence for a Higher-Order Topological Insulator in a Three-Dimensional Material Built from Van Der Waals Stacking of Bismuth-Halide Chains," *Nature Materials* 20 (2021): 473–479, https://doi.org/10.1038/s41563-020-00871-7.

11. A. M. Morales and C. M. Lieber, "A Laser Ablation Method for the Synthesis of Crystalline Semiconductor Nanowires," *Science* 279 (1998): 208–211, https://doi.org/10.1126/science.279.5348.208.

12. Y. R. Hacohen, R. Popovitz-Biro, E. Grunbaum, Y. Prior, and R. Tenne, "Vapor–Liquid–Solid (VLS) Growth of $NiCl_2$ Nanotubes via Reactive Gas Laser Ablation," *Advanced Materials* 14 (2002): 1075–1078.

13. R. Arenal, O. Stephan, J.-L. Cochon, and A. Loiseau, "Root-Growth Mechanism for Single-Walled Boron Nitride Nanotubes in Laser Vaporization Technique," *Journal of the American Chemical Society* 129 (2007): 16183–16189, https://doi.org/10.1021/ja076135n.

14. B. Lim, J. Wang, P. H. C. Camargo, C. M. Cobley, M. J. Kim, and Y. Xia, "Twin-Induced Growth of Palladium–Platinum Alloy Nanocrystals," *Angewandte Chemie International Edition* 48 (2009): 6304–6308, https://doi.org/10.1002/anie.200902235.

15. S. Li, Y.-C. Lin, W. Zhao, et al., "Vapour–Liquid–Solid Growth of Monolayer MoS_2 Nanoribbons," *Nature Materials* 17 (2018): 535–542, https://doi.org/10.1038/s41563-018-0055-z.

16. T. Chowdhury, J. Kim, E. C. Sadler, et al., "Substrate-Directed Synthesis of MoS_2 Nanocrystals with Tunable Dimensionality and Optical Properties," *Nature Nanotechnology* 15 (2020): 29–34, https://doi.org/10.1038/s41565-019-0571-2.

17. J. Li, W. Bi, W. Ki, X. Huang, and S. Reddy, "Nanostructured Crystals: Unique Hybrid Semiconductors Exhibiting Nearly Zero and Tunable Uniaxial Thermal Expansion Behavior," *Journal of the American Chemical Society* 129 (2007): 14140–14141, https://doi.org/10.1021/ja075901n.

18. X. Huang, M. Roushan, T. J. Emge, et al., "Flexible Hybrid Semiconductors with Low Thermal Conductivity: the Role of Organic Diamines," *Angewandte Chemie International Edition* 48 (2009): 7871–7874, https://doi.org/10.1002/anie.200903234.

19. X. Zhang, M. Hejazi, S. J. Thiagarajan, et al., "From 1D Chain to 3D Network: a New Family of Inorganic–Organic Hybrid Semiconductors $MO_3(L)_X$ (M = Mo, W; L = Organic Linker) Built on Perovskite-Like Structure Modules," *Journal of the American Chemical Society* 135 (2013): 17401–17407, https://doi.org/10.1021/ja4077556.

20. Y. Li, X. Jiang, Z. Fu, et al., "Coordination Assembly of 2D Ordered Organic Metal Chalcogenides with Widely Tunable Electronic Band Gaps," *Nature Communications* 11 (2020): 261, https://doi.org/10.1038/s41467-019-14136-8.

21. Y. Li, J. Yang, R. Zhao, et al., "Design of Organic–Inorganic Hybrid Heterostructured Semiconductors via High-Throughput Materials Screening for Optoelectronic Applications," *Journal of the American Chemical Society* 144 (2022): 16656–16666, https://doi.org/10.1021/jacs.2c07434.

22. H. Zhu, Y. Fu, F. Meng, et al., "Lead Halide Perovskite Nanowire Lasers with Low Lasing Thresholds and High Quality Factors," *Nature Materials* 14 (2015): 636–642, https://doi.org/10.1038/nmat4271.

23. S. Zhuo, J. Zhang, Y. Shi, Y. Huang, and B. Zhang, "Self-Template-Directed Synthesis of Porous Perovskite Nanowires at Room Temperature for High-Performance Visible-Light Photodetectors," *Angewandte Chemie International Edition* 54 (2015): 5693–5696, https://doi.org/10.1002/anie.201411956.

24. Z. Yuan, C. Zhou, Y. Tian, et al., "One-dimensional Organic Lead Halide Perovskites with Efficient Bluish White-light Emission," *Nature Communications* 8 (2017): 14051, https://doi.org/10.1038/ncomms14051.

25. J. Teeter, N. Y. Kim, T. Debnath, et al., "Achieving the 1D Atomic Chain Limit in Van der Waals Crystals," *Advance Material* 36 (2024): 2409898.

26. V. S. Larisa and N. V. Alexander, "Diverse Magnetic Chains in Inorganic Compounds," *Accounts of Material Research* 5 (2024): 836.

27. O. M. Yaghi, M. O'Keeffe, N. W. Ockwig, H. K. Chae, M. Eddaoudi, and J. Kim, "Reticular Synthesis and the Design of New Materials," *Nature* 423 (2003): 705–714, https://doi.org/10.1038/nature01650.

28. J. R. L. Hong-Cai Zhou and O. M. Yaghi, "Introduction to Metal–Organic Frameworks," *Chemical Reviews* 112 (2012): 673–674, https://doi.org/10.1021/cr300014x.

29. H. Furukawa, K. E. Cordova, M. O'Keeffe, and O. M. Yaghi, "The Chemistry and Applications of Metal-Organic Frameworks," *Science* 341 (2013): 974, https://doi.org/10.1126/science.1230444.

30. J. Zheng, Z. Lu, K. Wu, G.-H. Ning, and D. Li, "Coinage-Metal-Based Cyclic Trinuclear Complexes with Metal–Metal Interactions: Theories to Experiments and Structures to Functions," *Chemical Reviews* 120 (2020): 9675–9742, https://doi.org/10.1021/acs.chemrev.0c00011.

31. X.-N. Wang, P. Zhang, A. Kirchon, et al., "Crystallographic Visualization of Postsynthetic Nickel Clusters into Metal–Organic Framework," *Journal of the American Chemical Society* 141 (2019): 13654–13663, https://doi.org/10.1021/jacs.9b06711.

32. M. I. Gonzalez, A. B. Turkiewicz, L. E. Darago, et al., "Confinement of Atomically Defined Metal Halide Sheets in a Metal–organic Framework," *Nature* 577 (2020): 64–68, https://doi.org/10.1038/s41586-019-1776-0.

33. A. Turkiewicz, W. Tomlinson, M. I. Gonzalez, J. P. Hooper, and J. R. Long, “Templated Growth of a Spin-Frustrated Cluster Fragment of $MnBr_2$ in a Metal–Organic Framework,” *Inorganic Chemistry* 60 (2021): 16103–16110, https://doi.org/10.1021/acs.inorgchem.1c01345.

34. W. Zhang, H. Jiang, Y. Liu, et al., “Metal-halide Porous Framework Superlattices,” *Nature* 638 (2025): 418–424, https://doi.org/10.1038/s41586-024-08447-0.

35. J. A. Christians, R. C. M. Fung, and P. V. Kamat, “An Inorganic Hole Conductor for Organo-Lead Halide Perovskite Solar Cells. Improved Hole Conductivity with Copper Iodide,” *Journal of the American Chemical Society* 136 (2014): 758–764, https://doi.org/10.1021/ja411014k.

36. C. Yang, D. Souchay, M. Kneiß, et al., “Transparent Flexible Thermoelectric Material Based on Non-toxic Earth-abundant p-type Copper Iodide Thin Film,” *Nature Communications* 8 (2017): 16076, https://doi.org/10.1038/ncomms16076.

37. A. Liu, H. Zhu, W.-T. Park, et al., “High-performance p-channel Transistors with Transparent Zn Doped-CuI,” *Nature Communications* 11 (2020): 4309, https://doi.org/10.1038/s41467-020-18006-6.

38. A. Liu, H. Zhu, M.-G. Kim, J. Kim, and Y.-Y. Noh, “Engineering Copper Iodide (CuI) for Multifunctional p-Type Transparent Semiconductors and Conductors,” *Advanced Science* 8 (2021): 2100546, https://doi.org/10.1002/advs.202100546.

39. W. Liu, Y. Fang, and J. Li, “Copper Iodide Based Hybrid Phosphors for Energy-Efficient General Lighting Technologies,” *Advanced Functional Materials* 28 (2018): 1705593, https://doi.org/10.1002/adfm.201705593.

40. J. Troyano, F. Zamora, and S. Delgado, “Copper(i)–iodide Cluster Structures as Functional and Processable Platform Materials,” *Chemical Society Reviews* 50 (2021): 4606–4628, https://doi.org/10.1039/D0CS01470B.

41. J. He, J. Huang, Y. He, et al., “A Boiling-Water-Stable, Tunable White-Emitting Metal–Organic Framework from Soft-Imprint Synthesis,” *Chemistry—A European Journal* 22 (2016): 1597, https://doi.org/10.1002/chem.201504941.

42. S. Yao, X. Sun, B. Liu, et al., “Two Heterovalent Copper–organic Frameworks with Multiple Secondary Building Units: High Performance for Gas Adsorption and Separation and I_2 Sorption and Release,” *Journal of Materials Chemistry A* 4 (2016): 15081–15087, https://doi.org/10.1039/C6TA05142A.

43. S. L. Hou, J. Dong, X. L. Jiang, Z. H. Jiao, and B. Zhao, “A Noble-Metal-Free Metal–Organic Framework (MOF) Catalyst for the Highly Efficient Conversion of CO_2 with Propargylic Alcohols,” *Angewandte Chemie International Edition* 58 (2019): 577–581, https://doi.org/10.1002/anie.201811506.

44. W.-H. Fang and G.-Y. Yang, “Constructing Heterometallic Frameworks with Highly Connected Topology Based on Edge-to-edge Hexanuclear Lanthanide Clusters,” *CrystEngComm* 16 (2014): 1885–1892, https://doi.org/10.1039/c3ce42224k.

45. S. Mishra, E. Jeanneau, G. Ledoux, and S. Daniele, “Novel Barium–Organic Incorporated Iodometalates: Do They Have Template Properties for Constructing Rare Heterotrimetallic Hybrids?,” *Inorganic Chemistry* 53 (2014): 11721–11731, https://doi.org/10.1021/ic501963y.

46. Y.-Q. Xue, X. Yang, X.-L. Sun, Z.-Y. Han, J. Sun, and H. He, “Reversible Structural Transformation of Cu^{I} –Tb^{III} Heterometallic MOFs with Highly Efficient Detection Capability toward Penicillin,” *Inorganic Chemistry* 60 (2021): 11081–11089, https://doi.org/10.1021/acs.inorgchem.1c00952.

47. Z. F. Wu, C. Z. Wang, X. W. Liu, et al., “Confinement of 1D Chain and 2D Layered CuI Modules in K-INA-R Frameworks via Coordination Assembly: Structure Regulation and Semiconductivity Tuning,” *Journal of the American Chemical Society* 145 (2023): 19293–19302, https://doi.org/10.1021/jacs.3c05095.

48. B. Wolpert, M. Leitl, A. Pfitzner, and V. M. Mirsky, “Chemosensitive Properties of Electrically Conductive Cu(I) Compounds at Room Temperature,” *Sensors and Actuators B: Chemical* 134 (2008): 839–842, https://doi.org/10.1016/j.snb.2008.06.047.

49. B. Wolpert, O. S. Wolfbeis, and V. M. Mirsky, “Gas Sensing Properties of Electrically Conductive Cu(I) Compounds at Elevated Temperatures,” *Sensors and Actuators B: Chemical* 142 (2009): 446–450, https://doi.org/10.1016/j.snb.2009.04.042.

50. R.-Q. Zou, H. Sakurai, and Q. Xu, “Preparation, Adsorption Properties, and Catalytic Activity of 3D Porous Metal–Organic Frameworks Composed of Cubic Building Blocks and Alkali-Metal Ions,” *Angewandte Chemie International Edition* 45 (2006): 8086, https://doi.org/10.1002/anie.200690169.

51. R. S. Forgan, R. A. Smaldone, J. J. Gassensmith, et al., “Nanoporous Carbohydrate Metal–Organic Frameworks,” *Journal of the American Chemical Society* 134 (2012): 406–417, https://doi.org/10.1021/ja208224f.

52. H. A. Patel, T. Islamoglu, Z. Liu, et al., “Noninvasive Substitution of K^+ Sites in Cyclodextrin Metal–Organic Frameworks by Li^+ Ions,” *Journal of the American Chemical Society* 139 (2017): 11020–11023, https://doi.org/10.1021/jacs.7b06287.

53. Y. L. Huang, S. P. Chiu, Z. X. Zhu, Z. Q. Li, and J. J. Lin, “Variable-range-hopping Conduction Processes in Oxygen Deficient Polycrystalline ZnO Films,” *Journal of Applied Physics* 107 (2010): 041301.

54. Y. Wen, G.-E. Wang, X. Jiang, X. Ye, W. Li, and G. Xu, “A Covalent Organic–Inorganic Hybrid Superlattice Covered with Organic Functional Groups for Highly Sensitive and Selective Gas Sensing,” *Angewandte Chemie International Edition* 60 (2021): 19710, https://doi.org/10.1002/anie.202107185.

55. K. Zhu, Z. Cheng, S. Rangan, et al., “A New Type of Hybrid Copper Iodide as Nontoxic and Ultrastable LED Emissive Layer Material,” *ACS Energy Letters* 6 (2021): 2565–2574, https://doi.org/10.1021/acsenergylett.1c00993.

56. M. I. Saidaminov, V. Adinolfi, R. Comin, et al., “Planar-integrated Single-crystalline Perovskite Photodetectors,” *Nature Communications* 6 (2015): 8724, https://doi.org/10.1038/ncomms9724.

57. D. Shi, V. Adinolfi, R. Comin, et al., “Low Trap-state Density and Long Carrier Diffusion in Organolead Trihalide Perovskite Single Crystals,” *Science* 347 (2015): 519–522, https://doi.org/10.1126/science.aaa2725.

58. Q. Han, S.-H. Bae, P. Sun, et al., “Single Crystal Formamidinium Lead Iodide ($FAPbI_3$): Insight into the Structural, Optical, and Electrical Properties,” *Advanced Materials* 28 (2016): 2253–2258, https://doi.org/10.1002/adma.201505002.

59. B. L. Ouay, M. Boudot, T. Kitao, T. Yanagida, S. Kitagawa, and T. Uemura, “Nanostructuration of PEDOT in Porous Coordination Polymers for Tunable Porosity and Conductivity,” *Journal of the American Chemical Society* 138 (2016): 10088–10091, https://doi.org/10.1021/jacs.6b05552.

60. Y. F. Huang, W. C. Jiao, Z. M. Chu, et al., “Ultrasensitive Room Temperature Ppb-level NO_2 Gas Sensors Based on SnS_2/rGO Nanohybrids with P–N Transition and Optoelectronic Visible Light Enhancement Performance,” *Journal of Materials Chemistry C* 7 (2019): 8616–8625, https://doi.org/10.1039/C9TC02436K.

61. R. S. Chen, J. Wang, Y. Xia, and L. Xiang, “Near Infrared Light Enhanced Room-temperature NO_2 Gas Sensing By Hierarchical ZnO Nanorods Functionalized With PbS Quantum Dots,” *Sensors and Actuators B: Chemical* 255 (2018): 2538–2545, https://doi.org/10.1016/j.snb.2017.09.059.

62. H. N. Bai, H. Guo, C. Feng, et al., “A Room-temperature Chemiresistive NO_2Sensor Based On One-step Synthesized SnO_2 Nanospheres Functionalized With Pd Nanoparticles and rGO Nanosheets,” *Applied Surface Science* 575 (2022): 151698, https://doi.org/10.1016/j.apsusc.2021.151698.

63. K. Rui, X. Wang, M. Du, et al., “Dual-Function Metal-Organic Framework-Based Wearable Fibers for Gas Probing and Energy Storage,” *ACS Applied Materials & Interfaces* 10 (2018): 2837–2842, https://doi.org/10.1021/acsami.7b16761.

64. W. J. Yan, D. Y. Chen, H. R. Fuh, et al., "Photo-Enhanced Gas Sensing of SnS_2 With Nanoscale Defects," *RSC Advances* 9 (2019): 626.

65. D. Gu, X. Y. Wang, W. Liu, et al., "Visible-light Activated Room Temperature NO_2 Sensing of SnS_2 Nanosheets Based Chemiresistive Sensors," *Sensors and Actuators B: Chemical* 305 (2020): 127455, https://doi.org/10.1016/j.snb.2019.127455.

66. H. T. Wang, J. H. Bai, M. Dai, et al., "Visible Light Activated Excellent NO_2 Sensing Based on 2D/2D ZnO/G-C_3N_4 Heterojunction Composites," *Sensors and Actuators B: Chemical* 304 (2020): 127287, https://doi.org/10.1016/j.snb.2019.127287.

67. Y. Xia, C. Y. Hu, S. H. Guo, et al., "Sulfur-vacancy-enriched MoS_2 Nanosheets Based Heterostructures for near-infrared Optoelectronic NO_2 Sensing," *ACS Applied Nano Materials* 3 (2020): 665–673.

68. L. He, W. Y. Zhang, H. Y. Wu, and Y. Zhao, "Zn–Co Zeolitic Imidazolate Framework Nanoparticles Intercalated in Graphene Nanosheets for Room-Temperature NO_2 Sensing," *ACS Applied Nano Materials* 4 (2021): 3998.

69. H.-Z. Li, Y. Pan, Q. Li, et al., "Rationally Designed Titanium-based Metal-organic Frameworks for Visible-light Activated Chemiresistive Sensing," *Journal of Materials Chemistry A* 11 (2023): 965–971, https://doi.org/10.1039/D2TA08921A.

70. J. O. Kim, W. T. Koo, H. Kim, et al., "Large-area Synthesis of Nanoscopic Catalyst-decorated Conductive MOF Film Using Microfluidic-based Solution Shearing," *Nature Communications* 12 (2021): 4294, https://doi.org/10.1038/s41467-021-24571-1.

71. W.-T. Koo, J.-H. Cha, and J.-W. Jung, "Few-Layered WS_2 Nanoplates Confined in Co, N-Doped Hollow Carbon Nanocages: Abundant WS_2 Edges for Highly Sensitive Gas Sensors," *Advanced Functional Materials* 28 (2018): 1802575, https://doi.org/10.1002/adfm.201802575.

72. Z. Chen, H. Guo, F. Zhang, X. Li, J. Yu, and X. Chen, "Porous ZnO/rGO Nanosheet-Based NO_2 Gas Sensor with High Sensitivity and Ppb-Level Detection Limit at Room Temperature," *Advanced Materials Interfaces* 8 (2021): 2101511, https://doi.org/10.1002/admi.202101511.

73. D. Pandey, T. Samarth, V. K. Verma, et al., "Two-dimensional Cu(I)-MOF with Mesoporous Architecture towards Chemiresistive NO_2 Sensing," *Journal of Materials Chemistry A* 13 (2025): 11416, https://doi.org/10.1039/D4TA07702D.

74. W. Zhou, J. Jia, J. Lu, et al., "Recent Developments of Carbon-based Electrocatalysts for Hydrogen Evolution Reaction," *Nano Energy* 28 (2016): 29–43, https://doi.org/10.1016/j.nanoen.2016.08.027.

75. Y. Li, X. Jiang, Z. Fu, et al., "Coordination Assembly of 2D Ordered Organic Metal Chalcogenides with Widely Tunable Electronic Band Gaps," *Nature Communications* 11 (2020): 261, https://doi.org/10.1038/s41467-019-14136-8.

76. F. Yang, K. C. Donavan, S.-C. Kung, and R. M. Penner, "The Surface Scattering-Based Detection of Hydrogen in Air Using a Platinum Nanowire," *Nano Letters* 12 (2012): 2924, https://doi.org/10.1021/nl300602m.

77. S. Cui, H. Pu, S. A. Wells, et al., "Ultrahigh Sensitivity and Layer-dependent Sensing Performance of Phosphorene-based Gas Sensors," *Nature Communications* 6 (2015): 8632, https://doi.org/10.1038/ncomms9632.

78. S. Xu, H. Zhao, Y. Xu, R. Xu, and Y. Lei, "Carrier Mobility-Dominated Gas Sensing: a Room-Temperature Gas-Sensing Mode for SnO_2 Nanorod Array Sensors," *ACS Applied Materials & Interfaces* 10 (2018): 13895, https://doi.org/10.1021/acsami.8b03953.

79. M. Yin, K. Wang, L. Zhang, C. Gao, J. Ren, and L. Yu, "Ternary Alloyed $MoS_{2-x}Se_X$ Nanocomposites with a Carrier Mobility-dominated Gas Sensing Mode: a Superior Room Temperature Gas Sensing Material for NO_2 Sensors," *Journal of Materials Chemistry C* 11 (2023): 9715–9726, https://doi.org/10.1039/D3TC01551C.

80. K. Tan, S. Zuluaga, H. Wang, et al., "Interaction of Acid Gases SO_2 and NO_2 with Coordinatively Unsaturated Metal Organic Frameworks: M-MOF-74 (M = Zn, Mg, Ni, Co)," *Chemistry of Materials* 29 (2017): 4227–4235, https://doi.org/10.1021/acs.chemmater.7b00005.

81. J. Kang, J. Carnis, D. Kim, et al., "Time-resolved in Situ Visualization of the Structural Response of Zeolites during Catalysis," *Nature Communications* 11 (2020): 5901, https://doi.org/10.1038/s41467-020-19728-3.

82. W. Y. Qu, X. Fang, Z. H. Ren, et al., "NO Selective Catalytic Reduction over Atom-Pair Active Sites Accelerated via in Situ NO Oxidation," *Environmental Science & Technology* 57 (2023): 7858, https://doi.org/10.1021/acs.est.3c00461.

83. A. W. Aylor, S. C. Larsen, J. A. Reimer, and A. T. Bell, "An Infrared Study of no Decomposition over Cu-ZSM-5," *Journal of Catalysis* 157 (1995): 592–602, https://doi.org/10.1006/jcat.1995.1324.

84. K. Hadjiivanov, D. Klissurski, G. Ramis, and G. Busca, "Fourier Transform IR Study of NO_x Adsorption on a CuZSM-5 $DeNO_x$ Catalyst," *Applied Catalysis B: Environmental* 7 (1996): 251–262, https://doi.org/10.1016/0926-3373(95)00034-8.

85. K. I. Hadjiivanov, "IR Study of CO and NOx Sorption on Ag-ZSM-5," *Microporous and Mesoporous Materials* 24 (1998): 41–49, https://doi.org/10.1016/S1387-1811(98)00147-4.

86. K. I. Hadjiivanov, "Identification of Neutral and Charged N_XO_y Surface Species by IR Spectroscopy," *Catalysis Reviews* 42 (2000): 71, https://doi.org/10.1081/CR-100100260.

87. K. Nakamoto, "Infrared and Raman Spectra of Inorganic and Coordination Compounds," *Handbook of Vibrational Spectroscopy*, (2001).

88. S. Jensen, K. Tan, L. Feng, J. Li, H. C. Zhou, and T. Thonhauser, "Porous Ti-MOF-74 Framework as a Strong-Binding Nitric Oxide Scavenger," *Journal of the American Chemical Society* 142 (2020): 16562, https://doi.org/10.1021/jacs.0c02772.

89. J. A. Rodriguez, T. Jirsak, S. Sambasivan, D. Fischer, and A. Maiti, "Chemistry of NO_2 on CeO_2 and MgO: Experimental and Theoretical Studies on the Formation of NO_3," *The Journal of Chemical Physics* 112 (2000): 9929–9939, https://doi.org/10.1063/1.481629.

90. J. A. Rodriguez, T. Jirsak, J. Dvorak, S. Sambasivan, and D. Fischer, "Reaction of NO_2 with Zn and ZnO: Photoemission, XANES, and Density Functional Studies on the Formation of NO_3," *The Journal of Physical Chemistry B* 104 (2000): 319–328, https://doi.org/10.1021/jp993224g.

91. Z. Meng, R. M. Stolz, and K. A. Mirica, "Two-Dimensional Chemiresistive Covalent Organic Framework with High Intrinsic Conductivity," *Journal of the American Chemical Society* 141 (2019): 11929–11937, https://doi.org/10.1021/jacs.9b03441.

92. Y. Ma, X. Han, S. Xu, et al., "Atomically Dispersed Copper Sites in a Metal–Organic Framework for Reduction of Nitrogen Dioxide," *Journal of the American Chemical Society* 143 (2021): 10977–10985, https://doi.org/10.1021/jacs.1c03036.

93. M.-S. Yao, W.-X. Tang, G.-E. Wang, B. Nath, and G. Xu, "MOF Thin Film-Coated Metal Oxide Nanowire Array: Significantly Improved Chemiresistor Sensor Performance," *Advanced Materials* 28 (2016): 5229–5234, https://doi.org/10.1002/adma.201506457.

94. G. Kresse and J. Furthmüller, "Efficiency of ab-initio Total Energy Calculations for Metals and Semiconductors Using a Pane-Wave Basis Set," *Computational Material Science* 6 (1996): 15–50.

95. G. Kresse and J. Furthmüller, "Efficient Iterative Schemes for Ab Initio Total-energy Calculations Using a Plane-wave Basis Set," *Physical Review B* 54 (1996): 11169, https://doi.org/10.1103/PhysRevB.54.11169.

96. S. Grimme, J. Antony, S. Ehrlich, and H. Krieg, "A Consistent and Accurate Ab Initio Parametrization of Density Functional Dispersion Correction (DFT-D) for the 94 Elements H-Pu," *The Journal of Chemical Physics* 132 (2010): 154104, https://doi.org/10.1063/1.3382344.

97. G. M. Sheldrick, "Crystal Structure Refinement with SHELXL," *Acta Crystallographica Section C Structural Chemistry* 71 (2015): 3–8, https://doi.org/10.1107/S2053229614024218.

Supporting Information

Additional supporting information can be found online in the Supporting Information section.

Supporting File 1: adfm74077-sup-0001-SuppMat.docx.

Supporting File 2: adfm74077-sup-0002.zip.